Analytical Model of the Half-Bridge Series Resonant Inverter for Improved Power Conversion Efficiency and Performance

Héctor Sarnago, *Member, IEEE*, Óscar Lucía, *Senior Member, IEEE*, Arturo Mediano, *Senior Member, IEEE*, and José M. Burdío, *Senior Member, IEEE*

***Abstract*—Resonant power conversion is a key enabling technology of dc–dc conversion, inverters and contactless energy transfer systems. This paper presents an analytical model of the series resonant half-bridge topology aimed at improving the design, control, and efficiency of resonant power converters. The main contribution is a closed-form expression of the main converter waveforms as well as output power and efficiency. This model enables a fast design-space exploration, as well as the implementation of advanced control techniques using adaptive control or real-time emulation, significantly improving the converter operation. The analytical expressions presented have been applied and verified through a half-bridge series resonant inverter applied to induction heating applications, proving the accuracy and effectiveness of the proposed model.**

***Index Terms*—Analytical model, induction heating, inverter, resonant power conversion.**

NOMENCLATURE

R_L	Load resistance.
L_r	Resonant load inductance.
C_r	Resonant load capacitor.
$C_{\rm snb}$	Snubber capacitor.
V_s	Supply voltage.
v_o	Inverter output voltage.
v_c	Resonant capacitor voltage.
i_o	Load current.
$f_{\rm sw}$	Switching frequency.
$T_{\rm sw}$	Switching period.
D	Duty cycle.
ξ	Resonant tank damping factor.
ω_o	Resonant tank resonant frequency.
ω_n	Resonant tank natural frequency.
Q_o	Load quality factor.
λ	Exponential factor of the second-order differential equation.
r_i	Roots of the second-order differential equation.
f_i, g_i	Time-variant coefficients of the load current.
f_c, g_c	Time-variant coefficients of the resonant capacitor voltage.
f_o, g_o	Time-variant coefficients of the applied voltage.
$\mathbf{X_n}$	Matrix recurrence equation *n*th terms.
$\mathbf{A_n}$	Matrix recurrence equation *n*th proportional coefficients.
$\mathbf{B_n}$	Matrix recurrence equation *n*th independent coefficients.
P_o	Output power.
P_{on}	Conduction losses.
$P_{\rm sw}$	Switching losses.
η	Converter efficiency.
$S_{\rm H}$, $S_{\rm L}$	Equivalent switching devices.
$T_{\rm H}$, $T_{\rm L}$	Half-bridge transistors.
$D_{\rm H}$, $D_{\rm L}$	Half-bridge antiparallel diodes.
t	Time.
$t_{\rm snb}$	Snubber capacitor charge/discharge time.
t_d	Time between the transistor deactivation and the load current zero crossing.
t_{dt}	Dead time.
$v_{\rm on}$	Constant on-state voltage drop.
$r_{\rm on}$	Constant on-state series resistance.
i_T	Turn-off current.
β	Tail factor.
t_f	Fall time.
t_t	Tail time.
E	Energy in Δt interval.
Q	Stored charge.

Manuscript received June 3, 2014; revised August 10, 2014; accepted September 14, 2014. Date of publication September 19, 2014; date of current version March 5, 2015. This work was supported in parts by the Spanish MINECO under Projects TEC2013-42937-R, CSD2009-00046, and RTC-2014-1847-6, by the DGA-FSE, and by the Bosch and Siemens Home Appliances Group. Recommended for publication by Associate Editor M. Ordonez.

The authors are with the Department of Electronic Engineering and Communications, Universidad de Zaragoza, 50018 Zaragoza, Spain (e-mail: hsarnago@unizar.es; olucia@unizar.es; amediano@unizar.es; burdio@unizar.es).

Color versions of one or more of the figures in this paper are available online at http://ieeexplore.ieee.org.

Digital Object Identifier 10.1109/TPEL.2014.2359576

I. INTRODUCTION

RESONANT power converters are essential in many applications including high efficiency and power density dc–dc conversion, high-frequency inverters, and induction heating (IH) as well as contactless energy transfer (CET) systems, since they provide sinusoidal excitation with high power conversion efficiency. Among the available topologies, the series resonant full/half-bridge topology [1]–[4] is one of the most used topologies due to its good balance between cost, performance, and control complexity.

In the past, several research works have reported analyses of the series resonant half-bridge topology. Most of them provide steady-state results based on the Fourier transform [5], but in the form of an infinite sum of terms. As a consequence, it is not possible to obtain certain conclusions, such as the required modulation parameters to obtain some modulation profile, without

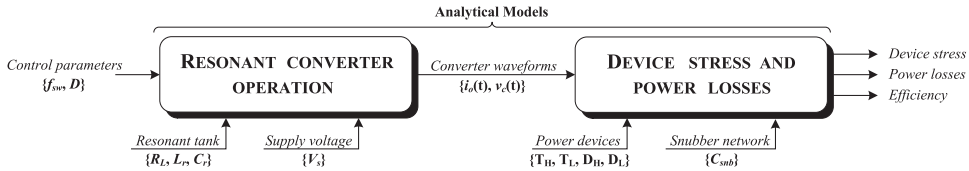

Fig. 1. Diagram of the proposed analytical models.

carrying out a massive parameter-variation simulation. Other analyses make some assumptions, such as considering the fundamental harmonic [6]–[8] approximation. However, this approach may not be accurate enough when high load variability is considered, typical of IH and CET systems. The nonresonant version of the half-bridge inverter, that is, considering infinite capacitance, is also analyzed in [9].

The improvement of circuit simulators and computing capabilities have also allowed several authors analyze the system response by the use of the state-space description [10]–[12], presenting the state matrix to perform a numeric simulation. However, several iterations are required, enlarging simulation times and reducing the chances of extracting useful design conclusions.

The objective of this paper is to develop an analytical model for the resonant inverter operation and the power converter losses. It enables a rapid evaluation of both transient and steady-state converter operation, including the resonant converter waveforms, devices stress, power losses, and efficiency. By using the proposed model, the impact of the power devices in the converter efficiency can be directly computed, enabling a further devices optimization process for a given set of restrictions. Consequently, the proposed model enables an easier and fast design space exploration taking into account important parameters of CET systems such as load coupling and variability, power converter operating point, and their influence on the efficiency and performance of the converter. Besides, having closed-form expression improves the converter operating point awareness and enables the implementation of real-time adaptive control schemes [13]–[17] and/or real-time emulation [18]–[21] taking advantage of modern digital control techniques. Consequently, both the design process and the operation of the resonant power converter can be significantly improved.

The proposed analytical model is based on a two-steps description model. In a first step, the resonant behavior of the converter is described in order to model the converter operation, neglecting the effect of the switching devices and the snubber network. Then, in a second step, the influence of the power devices on the converter efficiency, including snubber network, is analyzed. The flowchart of the proposed model is depicted in Fig. 1.

This paper is organized as follows. Section II performs the analysis of the resonant converter operation, and a closed-form expression of the resonant waveforms and the output power are obtained. Section III is focused on the analysis of the power devices effect in the converter losses, obtaining analytical expressions for the switching devices stress, power losses, and the converter efficiency. In order to verify the accuracy of the proposed model, the main simulation and experimental results are outlined in Section IV, and a design example taken advantage of the proposed model is detailed in Section V. Finally, the main conclusions of this paper are summarized in Section VI.

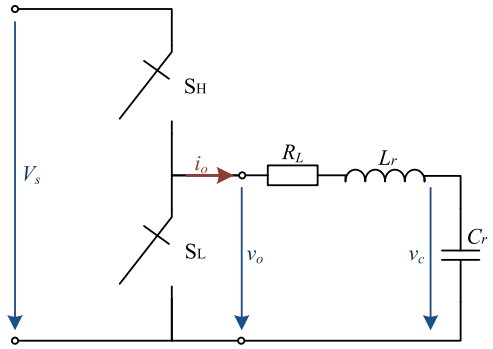

Fig. 2. Schematic of the series resonant half-bridge inverter.

II. Half-Bridge Series Resonant Converter Analysis

The half-bridge series resonant inverter (see Fig. 2) uses two bidirectional and unipolar ideal switches S_H and S_L, usually composed of a transistor with an antiparallel diode. The dc-link voltage V_s is applied to the resonant tank when S_H is activated, and oppositely, when $S_{\rm L}$ is activated, the resonant tank is short circuited. Thus, a complementary activation of the switches is assumed.

For this converter, a series *RLC* resonant tank is considered, composed of a load resistor, R_L, and the resonant elements, L_r and C_r. In the case of an IH applications, these elements model the induction load within a range of operating conditions [22]–[25], making this model simple and useful to obtain analytical and simulation results.

The analysis of the converter is based on its equivalent circuit and the following assumptions:

1) all passive elements are linear and time invariant;
2) a resonant operation mode with continuous conduction mode has been assumed;
3) ideal switching devices, S_H, S_L, have been assumed in the first step of the proposed analytical model, i.e., zero on-state voltage drop, infinite off-state resistance, and neglectable switching times.

The differential equation system that describes the dynamics of the resonant tank is defined by the current in the inductor i_o as follows:

$$R_L i_o(t) + L_r \frac{\mathrm{d}i_o(t)}{\mathrm{d}t} + \frac{1}{C_r}\int i_o(t)dt = v_o(t) \qquad (1)$$

where v_o is the output voltage applied to the resonant tank that equals V_s or 0 depending on the switches state. By defining $\xi = R_L/2L_r$ as the damping factor, and $\omega_o = 1/\sqrt{L_r C_r}$, $\omega_n = \sqrt{\omega_o^2 - \xi^2}$ as the resonant and natural angular frequencies, respectively, (1) can be rewritten as

$$\frac{\mathrm{d}^2 i_o(t)}{\mathrm{d}t^2} + 2\xi \frac{\mathrm{d}i_o(t)}{\mathrm{d}t} + \omega_o^2 i_o(t) = 0. \tag{2}$$

By assuming a solution in the form of $i_o(t) = e^{\lambda t}$, and a resonant operation mode, i.e., $\omega_o > \xi$, and $\xi < 1$, a family of solutions results

$$i_o(t) = (r_i e^{\lambda t} + \bar{r}_i e^{\bar{\lambda} t}) \tag{3}$$

where $\lambda = -\xi + j\omega_n$, and

$$r_i = \left(\frac{i_o(t=0)}{2}\right) + j\left(\frac{\xi}{2\omega_n} i_o(t=0) + \frac{1}{2L_r\omega_n}(v_c(t=0) - v_o(t=0))\right). \tag{4}$$

Thus, the load current can be expressed as

$$\begin{aligned} i_o(t) = \; & i_o(t=0) \underbrace{\left[e^{-\xi t}\left(\cos(\omega_n t) - \frac{\xi}{\omega_n}\sin(\omega_n t)\right)\right]}_{f_i(t)} \\ & + v_c(t=0) \underbrace{\left[e^{-\xi t}\left(\frac{-1}{L_r\omega_n}\sin(\omega_n t)\right)\right]}_{f_v(t)} \\ & + v_o(t=0) \underbrace{\left[e^{-\xi t}\left(\frac{1}{L_r\omega_n}\sin(\omega_n t)\right)\right]}_{f_o(t) = -f_v(t)} \end{aligned} \tag{5}$$

yielding

$$\begin{aligned} & i_o(t) = i_o(t=0) f_i(t) + v_c(t=0) f_v(t) + v_o(t=0) f_o(t) \\ & \begin{cases} f_i(t) = e^{-\xi t}\left(\cos(\omega_n t) - \dfrac{\xi}{\omega_n}\sin(\omega_n t)\right) \\ f_v(t) = e^{-\xi t}\left(\dfrac{1}{L_r\omega_n}\sin(\omega_n t)\right) = -f_o(t). \end{cases} \end{aligned} \tag{6}$$

Applying the same methodology, the resonant capacitor voltage v_c can be obtained as

$$\begin{aligned} & v_c(t) = i_o(t=0) g_i(t) + v_c(t=0) g_v(t) + v_o(t=0) g_o(t) \\ & \begin{cases} g_i(t) = e^{-\xi t}\left(\dfrac{1}{C_r\omega_n}\sin(\omega_n t)\right) \\ g_v(t) = e^{-\xi t}\left(\cos(\omega_n t) + \dfrac{\xi}{\omega_n}\sin(\omega_n t)\right) = 1 - g_o(t). \end{cases} \end{aligned} \tag{7}$$

The resonant waveforms can be obtained for each switching period *n* defined by the switching interval, t_n, and the constant voltage applied in each interval, $v_{o,n}(t) = V_{o,n}$ (see Fig. 3).

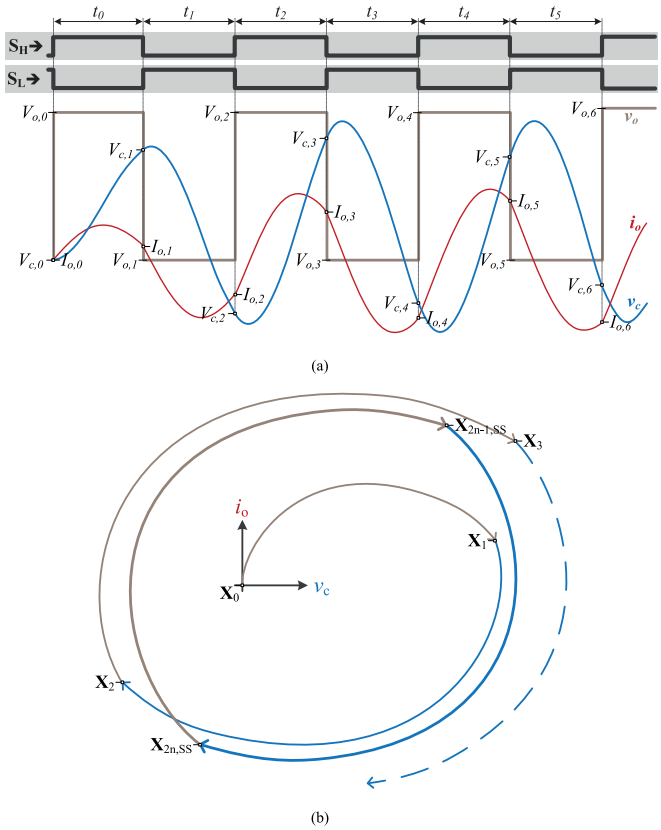

Fig. 3. Waveform transient for the series *RLC* resonant tank, where the dynamic oscillations are represented. (a) Main inverter waveforms and (b) state variable plane representation where the steady-state waveforms have been included.

Therefore, the initial conditions for each interval, $I_{o,n}$, $V_{c,n}$, results in a recurrence relation system

$$\begin{cases} I_{o,n} = I_{o,n-1} f_i(t_{n-1}) + V_{c,n-1} f_v(t_{n-1}) + v_{o,n-1} f_o(t_{n-1}) \\ V_{c,n} = I_{o,n-1} g_i(t_{n-1}) + V_{c,n-1} g_v(t_{n-1}) + v_{o,n-1} g_o(t_{n-1}). \end{cases} \tag{8}$$

These equations can be rewritten in the form of a matrix recurrence equation

$$\mathbf{X}_n = \mathbf{A}|_{n-1}\mathbf{X}_{n-1} + \mathbf{B}_{n-1} \tag{9}$$

where

$$\mathbf{X}_n = \begin{bmatrix} I_{o,n} \\ V_{c,n} \end{bmatrix}, \quad \mathbf{A}_n = \begin{bmatrix} f_i(t_n) & f_v(t_n) \\ g_i(t_n) & g_v(t_n) \end{bmatrix}$$

$$\mathbf{B}_n = v_{o,n}(t_n) \begin{bmatrix} f_o(t_n) \\ g_o(t_n) \end{bmatrix}. \tag{10}$$

In the case of the half-bridge converter, a universal modulation profile [7], [26], [27] can be defined by two parameters: the switching frequency f_{sw} (or equivalently the switching period $T_{\mathrm{sw}} = 1/f_{\mathrm{sw}}$) and the duty cycle *D* defined as the percentage of S_{H} activation in a switching period. Consequently, the switching

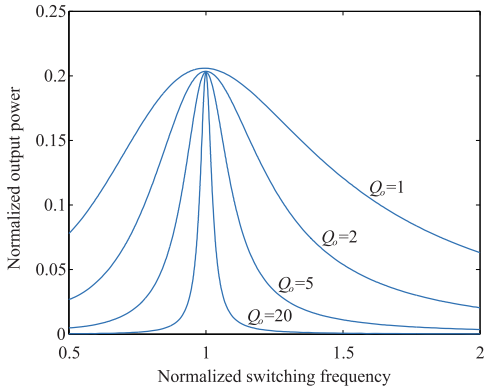

Fig. 4. Normalized output power, $P_n = P_o/(V_s^2/R_L)$, as a function of the load quality factor, $Q_o = \omega_o L_r/R_L$. Results for the normalized switching frequency variation, $f_{\rm sw}/(\omega_o/2\pi)$, by holding $D = 0.5$.

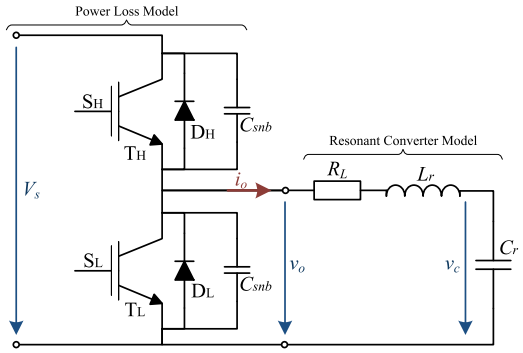

Fig. 5. Schematic of the complete power converter model.

intervals and the applied output voltage are

$$t_n = \begin{cases} DT_{\rm sw}, & n \text{ even} \\ (1-D)T_{\rm sw}, & n \text{ odd} \end{cases}, \quad v_{o,n}(t) = \begin{cases} V_s, & n \text{ even} \\ 0, & n \text{ odd.} \end{cases} \tag{11}$$

The steady-state solution $\mathbf{X}_{n,\rm SS}$ can be obtained by

$$\mathbf{X}_{n,\rm SS} = [\mathbf{I} - \mathbf{A}]^{-1}\mathbf{B} \tag{12}$$

leading to (13), shown at the bottom of the page. where $\varphi = \arctan(\omega_n/\xi)$. The output power (see Fig. 4) can be obtained by using the load current and the applied voltage across the resonant tank, yielding

$$\begin{aligned} P_o &= \frac{1}{T_{\rm sw}}\int_0^{T_{\rm sw}} v_o(t) i_o(t) dt \\ &= C_r V_s f_{\rm sw}(V_{c,2n+1,\rm SS} - V_{c,2n,\rm SS}). \end{aligned} \tag{14}$$

By holding the duty cycle to 50%, i.e., assuming a square-wave (SW) modulation (see Fig. 4) typical of most IH and CET systems, the output power expression can be simplified. Under these conditions, the maximum output power as a function of the switching frequency is

$$P_{o,D=0.5} = \frac{V_s^2}{R_L}\frac{\xi}{\pi\omega_o}\left(\frac{\sinh(\xi/2f_{\rm sw}) - \xi/\omega_n \sin(\omega_n/2f_{\rm sw})}{\cosh(\xi/2f_{sw}) + \cos(\omega_n/2f_{\rm sw})}\right). \tag{15}$$

Finally, the maximum output power $P_{o,\max}$ is obtained at $f_{\rm sw} = \omega_o/2\pi$, as a function of the load quality factor $Q_o = \omega_o L_r/R_L$, as

$$\begin{aligned} P_{o,\max} &= \frac{V_s^2}{R_L}\frac{1}{2\pi Q_o} \\ &\times \left(\frac{\sinh\left(\frac{\pi}{2Q_o}\right) - \frac{1}{\sqrt{4Q_o^2-1}}\sin\left(\pi\sqrt{1-\frac{1}{4Q_o^2}}\right)}{\cosh\left(\frac{\pi}{2Q_o}\right) + \cos\left(\pi\sqrt{1-\frac{1}{4Q_o^2}}\right)}\right). \end{aligned} \tag{16}$$

It is important to note that the model proposed in this section is valid to analyze transient and steady-state operation of the resonant converter operating under both zero-voltage switching (ZVS) and zero-current switching (ZCS) conditions, enabling a fast design space exploration under a wide operating conditions range.

III. Power Loss Model

Based on the previously presented analytical model of the half-bridge series resonant converter (see Fig. 5), a power loss model is introduced in this Section. This model is oriented to describe the main power losses in the converter, with a special emphasis in the power devices.

The bidirectional and unipolar equivalent switching devices S_H and S_L are usually composed of transistors T_H and T_L, featuring antiparallel diodes, D_H and D_L. A ZVS operation during turn ON is assumed in order to obtain high efficiency, with hard switching during the device turn OFF. Consequently, a lossless snubber network including a snubber capacitor, C_{snb}, in parallel with the switching device has been included in the power loss model. This capacitance includes the both the parasitic output capacitance of the switching devices and the external capacitance used to reduce the switching losses.

$$\begin{cases} I_{o,n,\rm SS} = (-1)^n \dfrac{V_S}{2L_r\omega_n}\dfrac{(\sin(T_{\rm sw}\omega_n) - \sin(T_{\rm sw}\omega_n D)e^{(-1)^{n+1}(1-D)T_{sw}\xi} - \sin(T_{\rm sw}\omega_n(1-D))e^{(-1)^n T_{\rm sw}\xi D})}{\cosh(T_{\rm sw}\xi) - \cos(T_{sw}\omega_n)} \\ V_{c,n,\rm SS} = (-1)^{n+1}\dfrac{V_s\omega_o}{2\omega_n}\left(\dfrac{\sin(T_{\rm sw}\omega_n + (-1)^{n+1}\varphi) - \sin(T_{\rm sw}\omega_n D + (-1)^{n+1}\varphi)e^{(-1)^{n+1}(1-D)T_{\rm sw}\xi} - \right. \\ \left. - \sin(T_{\rm sw}\omega_n(1-D) + (-1)^n\varphi)e^{(-1)^n T_{\rm sw}\xi D} + (-1)^n\frac{\omega_n}{\omega_o}e^{(-1)^n T_{\rm sw}\xi}}{\cosh(T_{\rm sw}\xi) - \cos(T_{\rm sw}\omega_n)}\right) + V_s \end{cases} \tag{13}$$

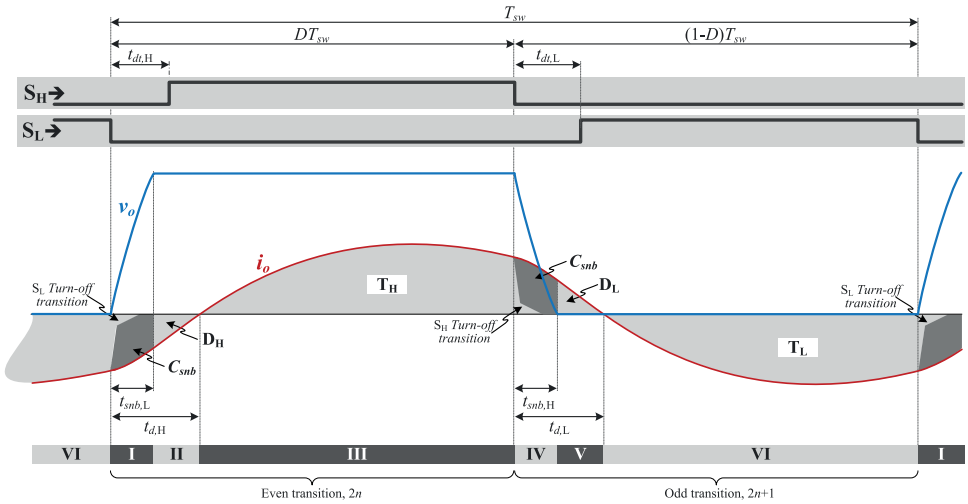

Fig. 6. Main waveforms of the converter operation assuming a soft-switching ZVS operation.

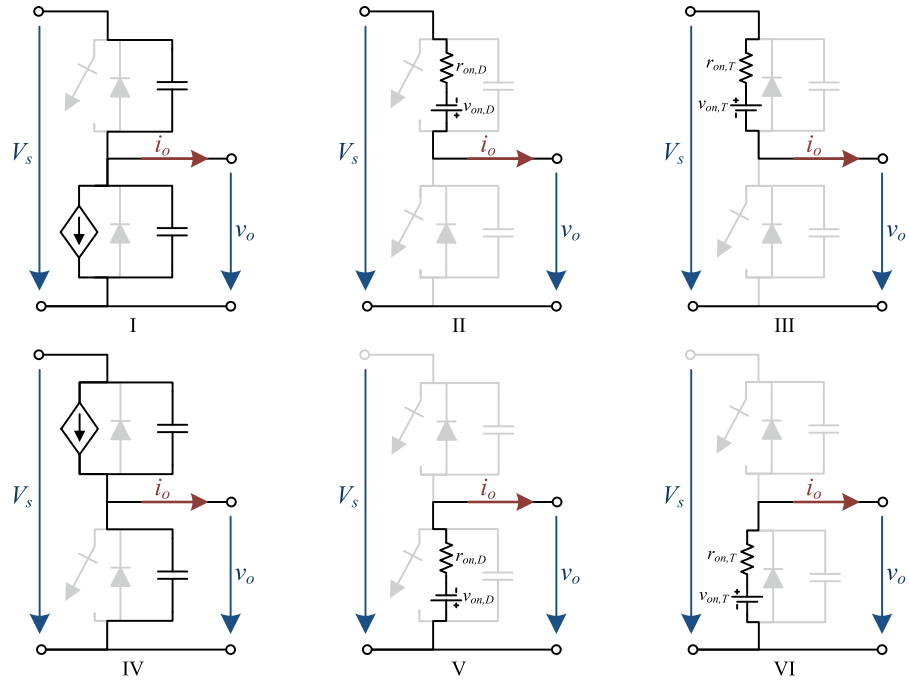

Fig. 7. Equivalent power loss model for the different circuit states. Equivalent models for the even transitions (I . . . III), and the odd transitions (IV . . . VI).

Considering the proposed power loss model, the main waveforms of the converter are depicted in Fig. 6. The converter operation has been divided into six different states (I–VI), depending on the current flow through the different power devices. States I–III correspond with even transitions computed in Section II, $\mathbf{X}_{2n}$, whereas the odd transitions, $\mathbf{X}_{2n+1}$, occurs during States IV–VI.

The proposed power loss model is based on the following assumptions:

1) *Conduction loss modeling:* The equivalent on-state model for the power devices is composed of a constant on-state voltage drop $v_{\mathrm{on},T}$ and $v_{\mathrm{on},D}$, and a series resistance $r_{\mathrm{on},T}$ and $r_{\mathrm{on},D}$, for the transistor and the antiparallel diode, respectively. Therefore, the on-state losses can be obtained by computing the average and rms current values.
2) *Off-state loss modeling:* The off-state leakage currents in the power devices are neglected.
3) *Switching losses:* Assuming ZVS soft-switching operation, the switching loss model is focused on the turn-off transition of the transistors, neglecting the turn-on losses in the antiparallel diodes. In order to compute the effect of the transistors in the switching losses, the turn-off transitions have been modeled using a piecewise function. Additionally, the effect of the parallel snubber capacitance, including both the parasitic and the external snubber capacitance, has been considered in the power loss model.

By considering these assumptions, the equivalent circuits are shown in Fig. 7. During states I and IV, the transistors S_H and S_L, respectively, are turned-off while the snubber capacitors are being charged/discharged. Consequently, the turn-off switching losses occur during these states. Once the snubber capacitors have been charged/discharged, the antiparallel diodes start conducting during states II and V, for $D_{\rm H}$ and $D_{\rm L}$, respectively, leading to a conduction loss term.

Afterwards, when the load current reaches zero, the transistors start conducting during states III and VI, respectively for $S_{\rm H}$ and $S_{\rm L}$, resulting in a conduction loss term. At this point, it is important to remark that the power transistor must be activated before the end of states II and V to ensure ZVS operation, i.e., $t_{{\rm snb},L} \leq t_{dt,H} < t_{d,H}$, $t_{{\rm snb},H} \leq t_{dt,L} < t_{d,L}$, for $S_{\rm H}$ and $S_{\rm L}$, respectively.

A. Conduction Losses

In order to compute the conduction losses, it is required to obtain a closed-form expression for both the average, $I_{\rm avg}$, and the rms, $I_{\rm rms}$, current values through the power devices. The device current can be directly obtained by means of the load current obtained in Section II during a certain conduction interval Δt. As a result, the average device current during the *n*th switching interval, $I_{{\rm avg},n}$ can be computed as

$$I_{{\rm avg},n}(\Delta t) = \frac{1}{T_{\rm sw}} \int\limits_{\Delta t} i_{o,n}(t)dt = C_r f_{\rm sw} v_{c,n}(\Delta t). \tag{17}$$

In order to obtain the rms current value, the following expression must be obtained

$$I_{{\rm rms},n}(\Delta t) = \sqrt{\frac{1}{T_{\rm sw}} \int\limits_{\Delta t} i_{o,n}^2(t)dt}. \tag{18}$$

To obtain the rms current expression, an energy balance analysis is performed. The rms current is directly related to the energy dissipated in the load resistor, $E_{r,n}$, yielding

$$E_{R,n} = \int\limits_{\Delta t} R_L i_{o,n}^2(t)dt = I_{{\rm rms},n}^2(\Delta t) R_L T_{\rm sw} \tag{19}$$

whereas the energy balance equation is $E_{R,n} + E_{C,n} + E_{L,n} = E_{o,n}$, resulting in

$$I_{{\rm rms},n}(\Delta t) = \sqrt{\frac{E_{o,n} - E_{C,n} - E_{L,n}}{T_{\rm sw} R_L}} \tag{20}$$

where the related energy terms are

$$\begin{cases} E_{C,n} = \dfrac{1}{2} C_r v_{c,n}^2(\Delta t) \\ E_{L,n} = \dfrac{1}{2} L_r i_{o,n}^2(\Delta t) \\ E_{o,n} = \displaystyle\int\limits_{\Delta t} v_{o,n}(t) i_{o,n}(t)dt = \frac{1}{2} V_s (1 + (-1)^n) C_r v_c(\Delta t). \end{cases} \tag{21}$$

Thus, both the average and the rms current values in the switching devices can be directly obtained for any switching pattern by a simply evaluation of the previously obtained values of the resonant capacitor voltage and the load current, during the different conduction intervals.

1) Antiparallel Diodes $D_{\rm H}$ and $D_{\rm L}$: The antiparallel diodes start conducting when the snubber capacitors are charged, i.e., during states II and V, yielding the conduction intervals $\Delta t_{\rm II} = [t_{{\rm snb},L},\ t_{d,H}]$ and $\Delta t_{\rm V} = [t_{{\rm snb},H},\ t_{d,L}]$ for D_H and D_L, respectively. Note that this model accurately accounts the conduction time of diodes, including the effect of the snubber capacitor.

The load current zero-crossing times $t_{d,H}$ and $t_{d,L}$ can be obtained by (6), yielding

$$\begin{cases} t_{d,H} = \dfrac{1}{\omega_n} \arctan\left(\dfrac{R_L \omega_n}{2\xi} \dfrac{I_{o,2n}}{V_{c,2n} - V_s} \right) \\ t_{d,L} = \dfrac{1}{\omega_n} \arctan\left(\dfrac{R_L \omega_n}{2\xi} \dfrac{I_{o,2n+1}}{V_{c,2n+1}} \right) \end{cases} \tag{22}$$

whereas the snubber charge/discharge time, $t_{\rm snb}$, directly depends on the operation conditions and the snubber capacitor value, further analyzed in Section III-B. By denoting the constant device on-state voltage drop $v_{{\rm on},D}$ and series resistance $r_{{\rm on},D}$, the power losses result

$$\begin{cases} P_{{\rm on},D_H} = v_{{\rm on},D} I_{{\rm avg},2n}(\Delta t_{\rm II}) + r_{{\rm on},D} I_{{\rm rms},2n}^2(\Delta t_{\rm II}) \\ P_{{\rm on},D_L} = v_{{\rm on},D} I_{{\rm avg},2n+1}(\Delta t_{\rm V}) + r_{{\rm on},D} I_{{\rm rms},2n+1}^2(\Delta t_{\rm V}). \end{cases} \tag{23}$$

2) Transistors $T_{\rm H}$ and $T_{\rm L}$: The power transistors start conducting when the load current cross the zero level, during states III and VI, thus the conduction intervals are $\Delta t_{\rm III} = DT_{\rm sw} - t_{d,H}$ and $\Delta t_{\rm VI} = (1-D)T_{\rm sw} - t_{d,L}$. By denoting the constant on-state voltage drop $v_{{\rm on},T}$ and a series resistance $r_{{\rm on},T}$, the power losses result

$$\begin{cases} P_{{\rm on},T_H} = v_{{\rm on},T} I_{{\rm avg},2n}(\Delta t_{\rm III}) + r_{{\rm on},T} I_{{\rm rms},2n}^2(\Delta t_{\rm III}) \\ P_{{\rm on},T_L} = v_{{\rm on},T} I_{{\rm avg},2n+1}(\Delta t_{\rm VI}) + r_{{\rm on},T} I_{{\rm rms},2n+1}^2(\Delta t_{\rm VI}). \end{cases} \tag{24}$$

B. Switching Losses

The ZVS is usually desired to reduce switching losses and limit d*v*/d*t* during the transitions. By doing so, the main switching losses occur in the power transistors T_H and T_L during the turn-off transition (states IV and I, respectively). It is important to note that this converter features snubber capacitors to reduce turn-off losses, and therefore, the $E_{\rm off}$ energy provided by the manufacturer of the power devices cannot be directly applied. As it is depicted in Fig. 8, the higher snubber capacitor, the reduced voltage slope, and consequently, a reduction in the turn-off term is appreciated. In this paper, a specific method to compute the turn-off losses in a ZVS resonant inverter with lossless snubber network is proposed (see Fig. 8).

The equivalent circuits during the turn-off transitions are shown in Fig. 7, states IV and I for T_H and T_L, respectively. They are composed by the series *RLC* resonant tank, the snubber capacitors, and a current source $i_{\rm T,off}$, which models

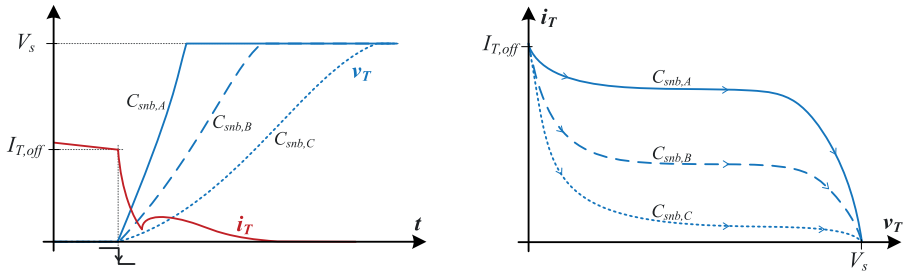

Fig. 8. Diagrams showing the turn-off transition for an IGBT for different snubber capacitances ($C_{\mathrm{snb},A} < C_{\mathrm{snb},B} < C_{\mathrm{snb},C}$). Temporal waveforms (a) versus transistor *i*–*v* diagram (b).

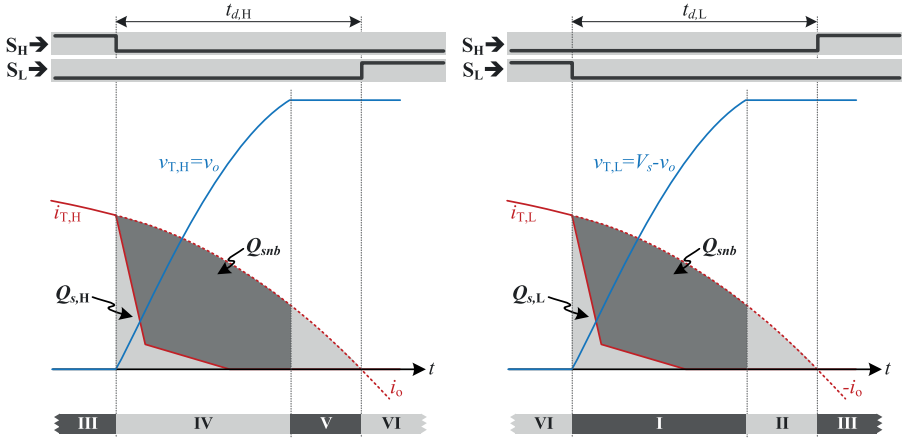

Fig. 9. Diagrams detailing the turn-off transition for (a) T_H and (b) T_L, respectively.

the transistor turn-off behavior. This current source depends on the power devices technology (e.g., IGBT or MOSFET) and the operation point (gating signals, device temperature, current level, and so on).

Linear piecewise models have been usually selected for simplicity [28], [29], using a single-interval model for MOSFET devices, defined by the current fall time $t_{f,i}$. In contrast, a two-intervals piecewise linear model is frequently employed in the IGBT devices in order to model the effect of the stored charge Q_s which results in the so-called IGBT current tail [19], [30]. The first interval is defined by a current fall time $t_{f,i}$, whereas the tail-effect occurs during the second one, defined by the current tail term $t_{t,i}$ and the tail factor β, $(0 \leq \beta \leq 1)$. In both cases, the device current at turn-off is denoted as $I_{T,\mathrm{off}}$, resulting

$$i_{T,\mathrm{off}}(t) = \begin{cases} I_{T,\mathrm{off}} \left(1 - \dfrac{\beta}{t_{f,i}} t\right), (0 \leq t < t_{f,i}) \\ I_{T,\mathrm{off}} (1-\beta) \left(1 - \dfrac{t - t_{f,i}}{t_{t,i}}\right), (t_{f,i} \leq t \leq t_{f,i} + t_{t,i}). \end{cases} \tag{25}$$

In order to make a general analysis, the IGBT model will be considered in this paper, being compatible for MOSFET devices by doing $\beta = 1$. By applying a charge balance analysis (see Fig. 9), the snubber charge, $Q_{\mathrm{snb}} = 2C_{\mathrm{snb}}V_s$, yielding an upper limit, $Q_{\mathrm{snb}} \leq Q_{o,\mathrm{off}} - Q_s$, where the load charge result

$$Q_{o,\mathrm{off}} = q_{o,\mathrm{off}}(t_d) = \int_{t_d} i_o(t)dt = C_r(v_c(t_d) - v_c(0)). \tag{26}$$

On the other hand, the temporal variation of the power device stored charge is

$$\begin{aligned} q_s(t) &= \int i_{T,\mathrm{off}}(t)dt \\ &= I_{T,\mathrm{off}} \begin{cases} \left(1 - \frac{\beta}{2t_{f,i}} t\right) t, (0 \leq t < t_{f,i}) \\ (1-\beta) \frac{(t_{f,i} + t_{t,i} - t)^2}{2t_{t,i}}, (t_{f,i} \leq t \leq t_{f,i} + t_{t,i}) \end{cases} \end{aligned} \tag{27}$$

yielding the total storage charge $Q_s = q_s(t_{f,i} + t_{f,i}) = (I_{T,\mathrm{off}}/2)[t_{f,i}(2-\beta) + t_{t,i}(1-\beta)]$. By using (26) and (27) in the charge balance equation, and solving for T_H and T_L, the maximum snubber capacitor to achieve ZVS results

$$C_{\mathrm{snb,max}} = \frac{C_r(v_c(t_d) - v_c(0)) - Q_s}{2V_s}. \tag{28}$$

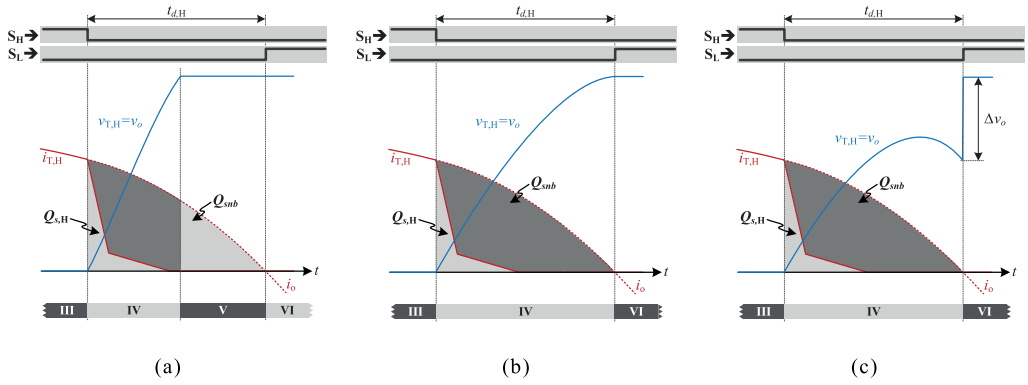

Fig. 10. Turn-off transition for T_H as a function of the snubber capacitor. (a) Reduced snubber capacitor, (b) optimum snubber capacitor, and (c) larger snubber capacitor.

In order to evaluate the switching losses, three different situations can be distinguished (see Fig. 10):

1) a reduced snubber capacitor value, $C_{\rm snb} < C_{{\rm snb},max}$ [see Fig. 10(a)];
2) the optimum snubber capacitor, $C_{\rm snb} = C_{\rm snb,max}$ [see Fig. 10(b)], also known as Class DE operation mode, which achieves minimum switching losses, in this mode, both the voltage (ZVS) and the current (ZVDS) at the turn-on transition are zero, being possible to neglect the diode conduction (States V, II, respectively);
3) a larger snubber capacitor value, $C_{\rm snb} > C_{\rm snb,max}$ [see Fig. 10(c)] causes an additional switching loss energy term in the form of $C_{\rm snb}\Delta v_o^2$. This mode must be avoided in order to limit losses and peak current in the switching devices.

Consequently, the switching losses, $P_{\rm sw,off}$, can be obtained by

$$P_{\rm sw,off} = f_{\rm sw}E_{\rm off} = f_{\rm sw}\int_{t_d} i_{T,\rm off}(t)v_o(t)dt = \frac{f_{\rm sw}}{2C_{snb}}\int_{t_d} i_{T,\rm off}(t)[\int i_o(t) - i_{T,\rm off}(t)dt]dt \tag{29}$$

$$P_{\rm sw,off} = \frac{f_{\rm sw}}{2C_{snb}}\int_{t_d} i_{T,\rm off}(t)[q_{o,\rm off}(t) - q_s(t)]dt \tag{30}$$

$$P_{\rm sw,off} = f_{\rm sw}\frac{C_r}{2C_{\rm snb}}\left[\left(\int_{t_d} i_{T,\rm off}(t)v_c(t)dt\right) - (v_c(0)Q_s) - \left(\frac{I_{T,\rm off}^2}{8C_r}\begin{pmatrix} t_{f,i}^2(2-\beta)^2 + t_{t,i}^2(1-\beta)^2 \\ +t_{f,i}t_{t,i}(4-2\beta)(1-\beta)\end{pmatrix}\right)\right]. \tag{31}$$

The integral term can be solved using integration by parts

$$\int i_{T,\rm off}(t)v_c(t)dt = i_{T,\rm off}(t)\int v_c(t)dt - \int\left(\frac{di_{T,\rm off}(t)}{dt}\int v_c(t)dt\right)dt \tag{32}$$

where using piecewise linear functions, the $di_{T,\rm off}(t)/dt$ term results constant, yielding

$$\int i_{T,\rm off}(t)v_c(t)dt = i_{T,\rm off}(t)\int v_c(t)dt - \frac{di_{T,\rm off}(t)}{dt}\int(\int v_c(t)dt)dt. \tag{33}$$

By applying KVL to the converter

$$\begin{cases}\int\left(\int v_c(t)dt\right)dt = \frac{V_s}{2}t^2 - L_rC_rv_c(t) - R_LC_r\int v_c(t)dt \\ \int v_c(t)dt = tV_s - L_ri_o(t) - R_LC_rv_c(t)\end{cases} \tag{34}$$

the integral term results

$$\int i_{T,\rm off}(t)v_c(t)dt = \frac{I_{T,\rm off}}{\omega_o^2}\begin{bmatrix} R_L\left(\left[\frac{\omega_o^2}{2\xi} - \Gamma_0\right]i_o(0) + [\Gamma_f]\,i_o(t_{f,i}) \right. \\ \left. +[\Gamma_{f+t}]i_o(t_{f,i}+t_{t,i})\right) \\ +\left(4\frac{\xi^2}{\omega_o^2} - 1\right)\left(\left[-\frac{\xi\omega_o^2}{2\omega_n^2} - \Gamma_0\right]v_c(0) + [\Gamma_f]\right. \\ \left.\times v_c(t_{f,i}) + [\Gamma_{f+t}]\,v_c(t_{f,i}+t_{t,i})\right) \\ +\left[\frac{\omega_o^2}{2}\Gamma_s - 2\xi\right]v_o(0)\end{bmatrix} \tag{35}$$

where

$$\Gamma_0 = \frac{\beta}{t_{f,i}}, \Gamma_f = \frac{(t_{f,i}(\beta-1)+\beta t_{t,i})}{t_{f,i}t_{t,i}}, \Gamma_{f+t} = \frac{(1-\beta)}{t_{t,i}}, \quad \text{and } \Gamma_s = t_{f,i}(2-\beta) + t_{t,i}(1-\beta). \tag{36}$$

Consequently, the switching losses can be easily calculated as a function of the power device switching parameters, the snubber capacitor, and the resonant tank.

IV. Simulation and Experimental Results

In order to verify the proposed analytical models, both SPICE simulations and experimental results have been compared.

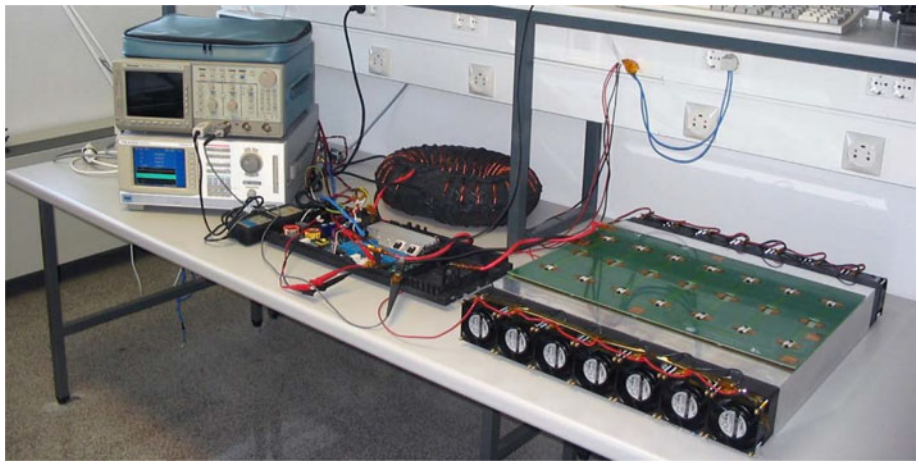

Fig. 11. Experimental prototype test-bench: power converter and discrete *RL* load.

TABLE I
PROTOTYPE PARAMETERS

	Components	Values
$R_{\rm eq}$	Load resistance	2.85 Ω
$L_{\rm eq}$	Equivalent inductance	19.5 μH
V_s	Supply voltage	230 V
C_r	Resonant capacitor	1440 nF
C_{snb}	Snubber capacitor	2×22nF
$S_{\rm H}$, $S_{\rm L}$	Switching devices (IGBTs)	GP4068D

Induction heating has been selected as a reference application of contactless energy transfer with a significant domestic and industrial relevance. It is important to note that, since closed-form expressions are obtained for both the main converter waveforms and the efficiency analysis, they can be computed using any mathematic software. In this case, MATLAB has been used to enable a fast design space exploration in order to optimize the desired performance and efficiency.

The prototype designed and built is based on a half-bridge series resonant inverter designed to supply an induction heating load [31] (see Fig. 11). The induction load is modeled as the series connection of an equivalent resistor $R_{\rm eq}$ and an equivalent inductor $L_{\rm eq}$ [32]. Consequently, a discrete power inductor and resistor have been used to avoid nonidealities of induction heating loads and provide an accurate verification of the model. The equivalent load resistance value is 2.85 Ω and the equivalent series inductance is 19.5 μH [33], [34]. These parameters accounts for both the coil and the induction load effect. The resonant capacitor has been chosen to obtain a 30-kHz resonant frequency to avoid the audible range [35], [36] while keeping low switching losses. Additional design parameters can be found in Table I.

A. Resonant Converter Operation Model

In order to verify the proposed analytical model, the main converter waveforms under different operating points have been compared using SPICE simulations and experimental results (see Fig. 12). These results include the converter operation at nominal duty cycle, $D = 0.5$, close to the resonant frequency [see Fig. 12(a) and (b)] and at high switching frequency [see Fig. 12(c) and (d)]. Additionally, the converter operation at $D = 0.75$ for $f_{\rm sw} = 50$ kHz has been included in [Fig. 12(e) and (f)]. From these results, it can be concluded that the analytical results are in good agreement with both the SPICE simulations and the experimental results, validating the accuracy of the proposed model under real operating conditions.

One of the key points of the proposed model is the feasibility to model transients and complex modulation patterns during the converter operation. Fig. 13 shows an eight-interval modulation pattern selected to test the proposed analytical model. The same modulation pattern has been evaluated using the proposed analytical model, obtaining the results shown in Fig. 14 for the load current (a) and resonant capacitor voltage (b). The good agreement between the experimental and the analytical model results proves the feasibility of the proposed model to predict the converter behavior either under variable modulation pattern or loads, typical of CET systems. Consequently, unlike previous analytical models based on the Fourier transform or first-harmonic approach, the proposed model proves to allow reproducing complex transient operations.

B. Power Loss Model

One of the most relevant issues of the power loss model is the turn-off losses model considering a ZVS soft-switching behavior, including the effect of the snubber capacitors for reduce the switching losses. Typical turn-off transitions are depicted in Fig. 15, using a snubber capacitance of 44 nF for $f_{\rm sw} = 50$ kHz (a) and $f_{\rm sw} = 75$ kHz (b).

In order to prove the feasibility of the proposed model, both the linear piecewise model for the IGBT current during the turn-off transition and the transistor voltage slope considering the snubber capacitance are depicted in Fig. 16. The linear piecewise parameters are $t_{f,i} = 58$ ns, $t_{t,i} = 402$ ns, and $\beta = 0.82$.

Finally, the instantaneous turn-off losses are shown in Fig. 17, comparing the experimental results with the predicted ones. The

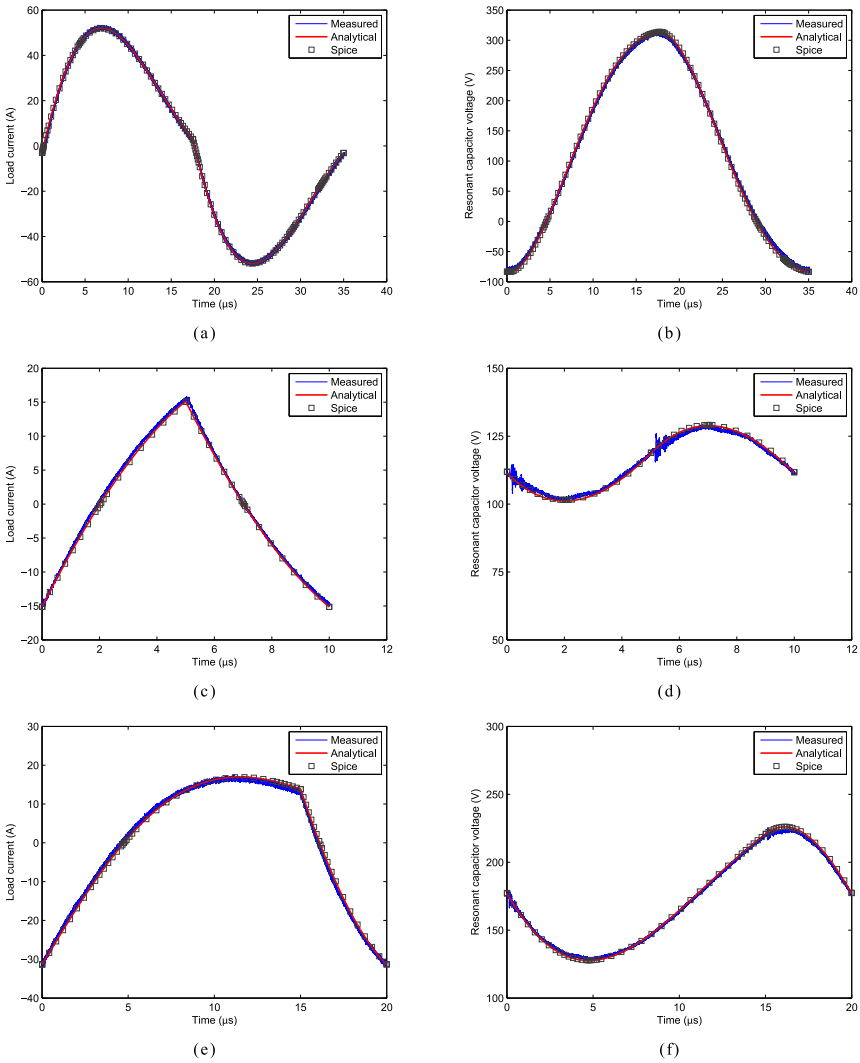

Fig. 12. Experimental and SPICE results versus predicted waveforms (load current and resonant capacitor voltage) using the proposed analytical model. Results at nominal duty cycle close to the resonant frequency at $f_{\rm sw} = 28.57$ kHz, and high operating frequency, $f_{\rm sw} = 100$ kHz (c-d). Results at $f_{\rm sw} = 50$ kHz for $D = 0.75$ (e-f).

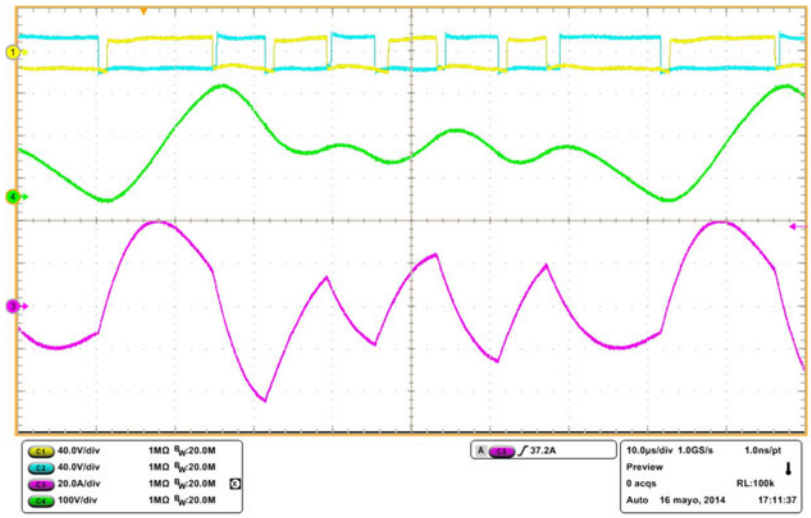

Fig. 13. Experimental waveforms of complex transient modulation pattern composed of eight different intervals. From top to bottom: gating signals (40 V/div), resonant capacitor voltage (100 V/div), and load current (20 A/div). Time 10 μs/div.

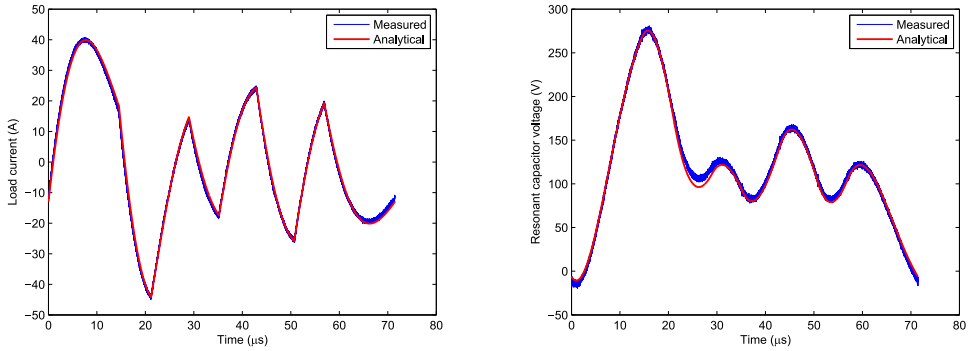

(a) (b)

Fig. 14. Theoretical versus experimental results for an arbitrary modulation pattern. (a) Load current and (b) resonant capacitor voltage.

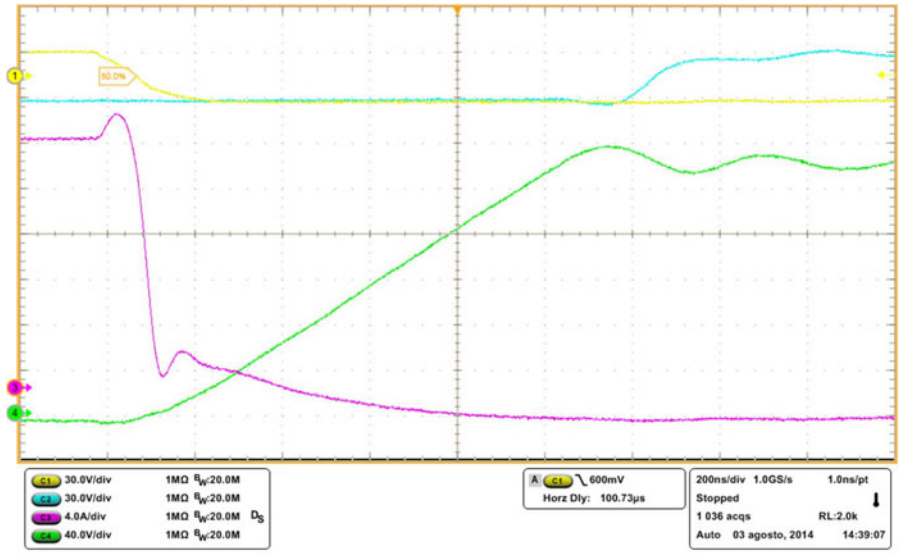

(a)

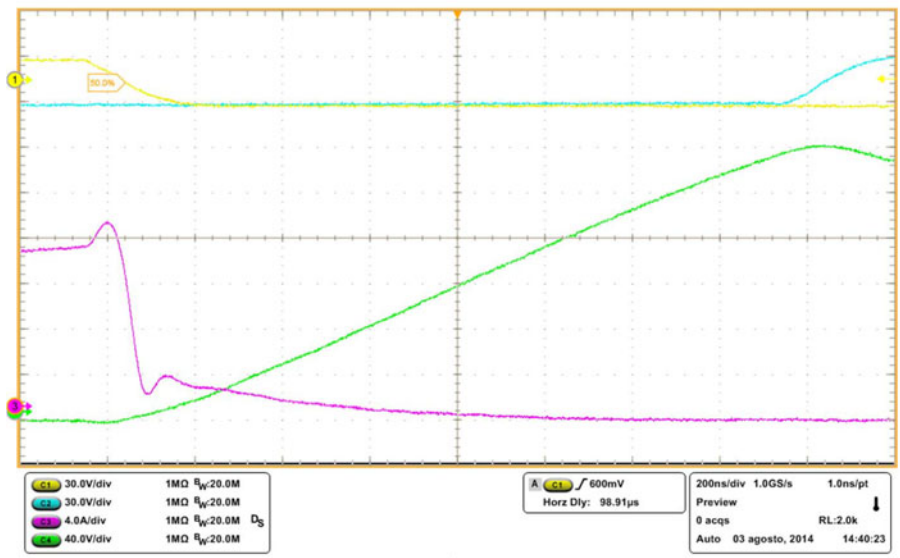

(b)

Fig. 15. Turn-off transition using IGBT devices at (a) $f_{\mathrm{sw}} = 50$ kHz and (b) 75 kHz. Results for a ZVS soft-switching behavior using $C_{\mathrm{snb}} = 44$ nF. From top to bottom: gating signals (30 V/div), transistor current (4 A/div), and voltage (40 V/div). Time 200 ns/div.

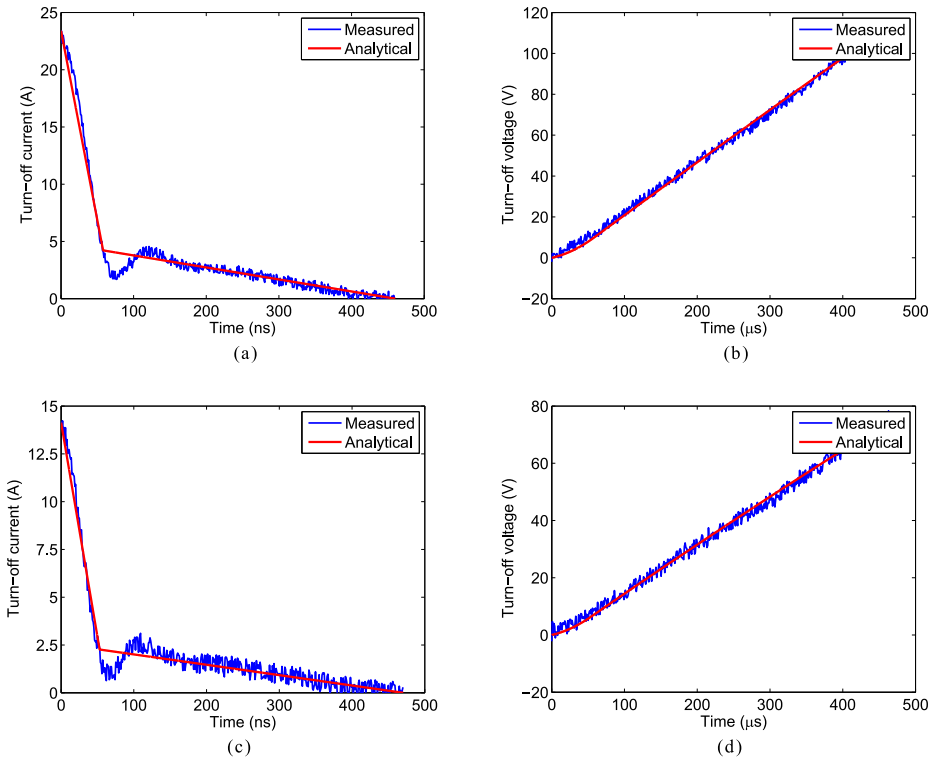

Fig. 16. Experimental versus analytical waveforms during the turn-off transition for a ZVS soft-switching behavior. (a, c) Transistor current and (b, d) transistor voltage for (a, b) $f_{\rm sw} = 50$ kHz and (c, d) $f_{\rm sw} = 75$ kHz.

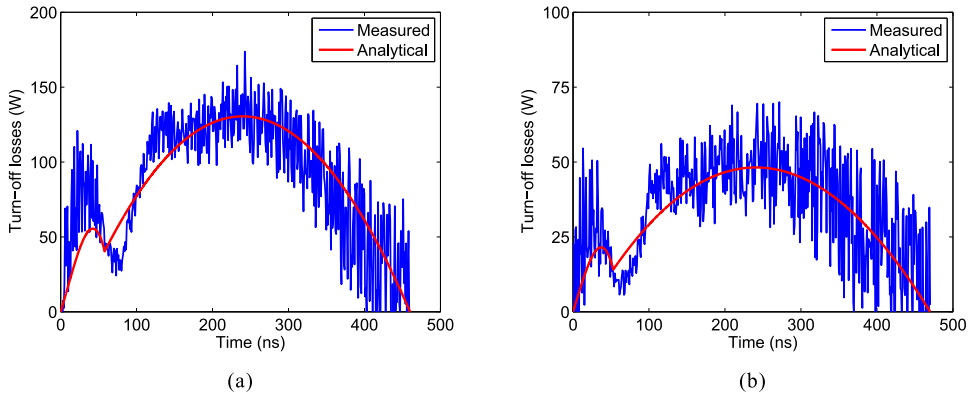

Fig. 17. Instantaneous turn-off losses. Experimental results versus analytical model for (a) $f_{\rm sw} = 50$ kHz and (b) $f_{\rm sw} = 75$ kHz.

predicted turn-off switching losses energy results 39.60 and 15.05 μJ, whereas the measured results is 39.87 and 15.91 μJ for $f_{\rm sw} = 50$ and 75 kHz, respectively. As a result of this, the simple piecewise model results reasonable for predicting the turn-off losses under ZVS soft-switching behavior.

Finally, in order to validate the complete power loss model, the on-state losses have been considered. The on-state parameters for the selected IGBTs copacked with antiparallel diodes are $V_{{\rm on},T} = 1.32$ V and $R_{{\rm on},T} = 34$ mΩ for the transistor, and $V_{{\rm on},D} = 1.08$ V and $R_{{\rm on},D} = 17$ mΩ for the antiparallel diode. Both the on-state losses and the switching losses as a function of the switching frequency using the proposed model are depicted in Fig. 18(a). Finally, the converter efficiency has been measured using a digital power analyzer (Yokogawa PZ4000) and compared with the predicted one using the analytical model in Fig. 18(b). These results validate the accuracy of the model not only to estimate current and voltage waveforms, but also to predict the converter efficiency, enabling further optimization.

V. Design Example: Series Resonant Inverter for IH

In this section, an example of resonant converter design and optimum device selection is provided taking advantage of the proposed model. The design flowchart, depicted in Fig. 19, is divided into two sections: the resonant load design, and afterwards, the power losses computation for optimum device

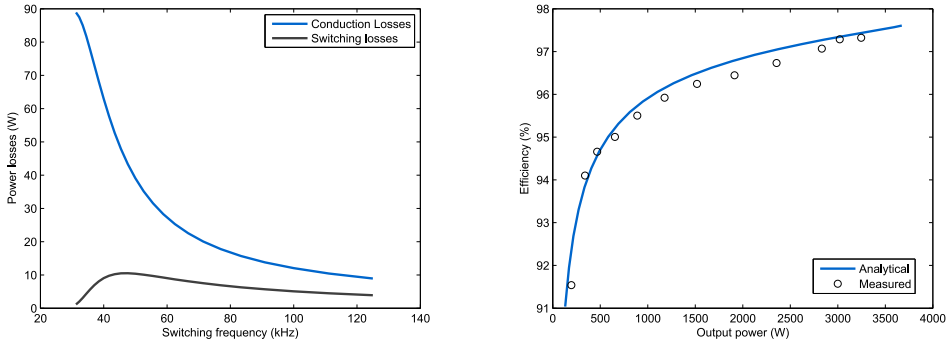

(a) (b)

Fig. 18. (a) Predicted converter losses detailing on-state losses and switching losses as a function of the switching frequency. (b) Theoretical versus experimental efficiency results.

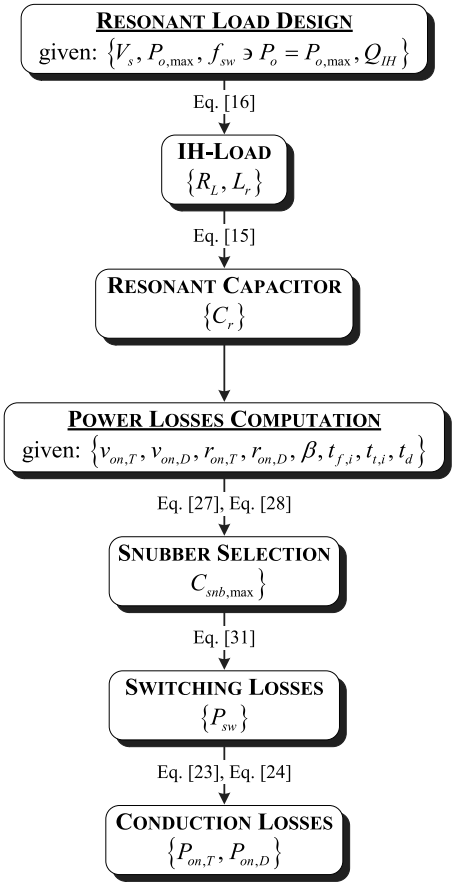

Fig. 19. Design flowchart using the proposed analytical model.

selection. In order to design the resonant converter, the main requirements are the following: supply voltage, $V_s = 300$ V, maximum output power, $P_{o,\max} = 1$ kW at 500 kHz switching frequency, which is suitable for hardening processes or low-resistivity metal heating. Considering the induction heating application, i.e., geometry and operating frequency, the induction heating load quality factor results $Q_{\rm IH} = 4.64$.

The first step consists on obtaining the equivalent IH-load parameters. By using (16), and assuming a 10% safety margin in the maximum output power, the IH-load resistance results, $R_L = 16.59\ \Omega$. Then, by using the quality factor definition, the equivalent IH-load inductance is obtained, i.e., $L_r = 24.5\ \mu$H. In order to obtain the required output power (1 kW) at the desired switching frequency (500 kHz), the resonant capacitor must be carefully selected. By using (15), the resonant capacitor results $C_r = 4.38$ nF, leading to a 4.4-nF commercial value. At this point, it is important to note that (15) results into two possible capacitor values: the lower one yields to the capacitive region of the resonant tank, i.e., ZCS switching behavior, whereas the selected one results in an inductive behavior, enabling a ZVS operation. Fig. 20(a) shows both the simulated and the measured output power curve as a function of the switching frequency.

TABLE II
POWER DEVICE CHARACTERISTICS

	Parameter	IHW40N60R	IKW75N60T
$v_{\rm on,T}$	Transistor on-state voltage drop	1.3 V	1.05 V
$r_{\rm on,T}$	Transistor on-state resistance	11.5 mΩ	7.5 mΩ
$v_{\rm on,D}$	Diode on-state voltage drop	1.4 V	1.1 V
$r_{\rm on,D}$	Diode on-state resistance	8.5 mΩ	6 mΩ
$t_{f,i}$	Current fall-time	39 ns	65 ns
$t_{t,i}$	Current tail-time	101 ns	190 ns
β	Tail factor	0.55	0.5

The second step deals with the power device selection. First, it is required to obtain the maximum snubber capacitance based on the power device switching parameters by using the charge-balance equation (28). At this point, it is important to note that the higher the snubber capacitance is, the lower the switching losses result. For that reason, the maximum snubber capacitance will be selected for the required maximum output power, yielding to a Class DE operation mode, i.e., a ZVS and ZDVS operation. It is also important to note that low switching speed devices will reduce the maximum snubber capacitance, notably increasing the switching losses. Thus, a high speed trench-gate and field-stop technology IGBT devices have been selected for this comparison. Their main characteristics are summarized in Table II. By holding the maximum delay time, $t_d = 10\%$, the maximum snubber capacitor (28) results 1.6 and 0.97 nF for the IHW40N60R and IKW75N60T, respectively.

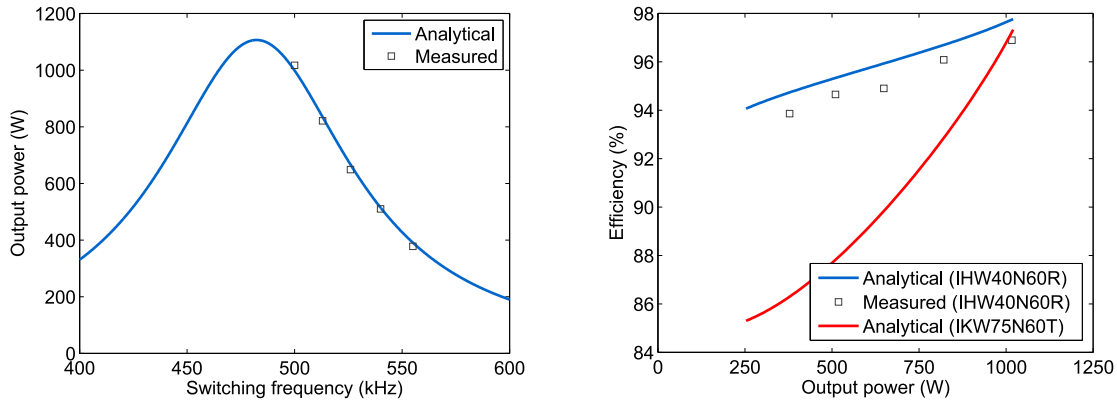

(a) (b)

Fig. 20. (a) Output power curve and (b) efficiency comparison using the proposed analytical model.

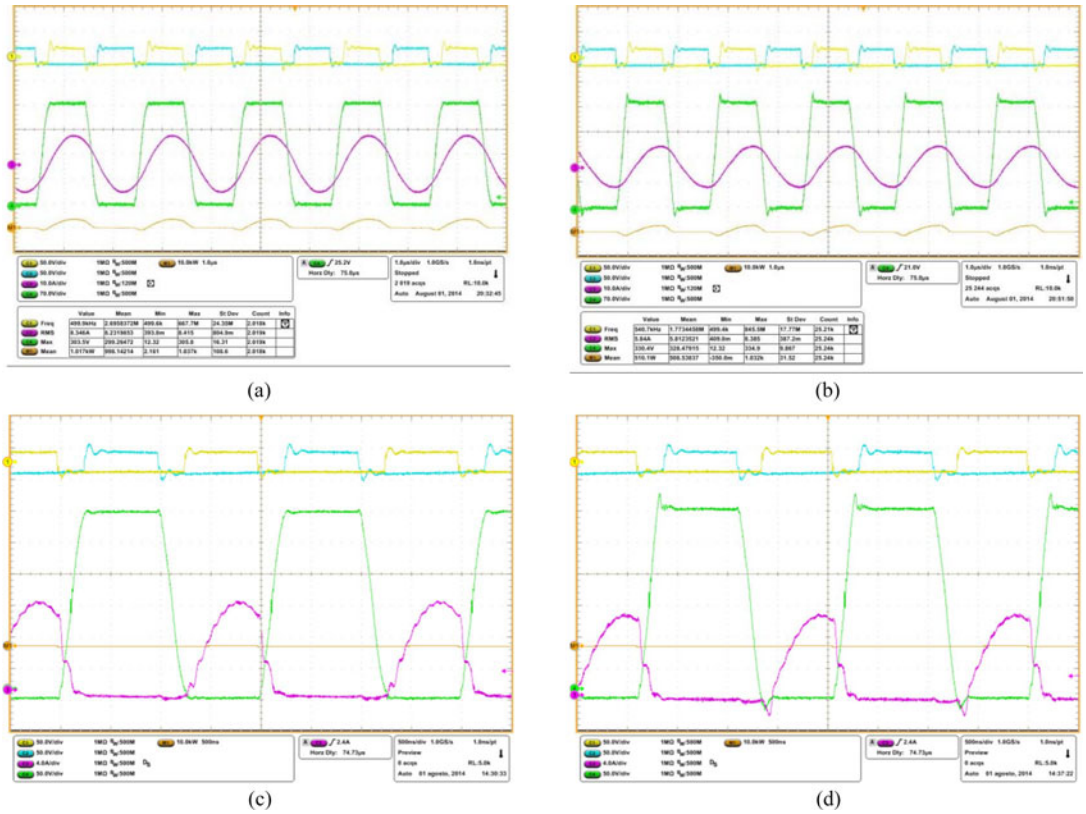

Fig. 21. (a, b) Main waveforms and (c, d) switching details of the designed converter taking advantage of the proposed analytical model at (a, c) 1 kW and (b, d) 0.5 kW.

Once the snubber capacitors have been selected, the switching losses can be directly computed using (31). Finally, conduction losses can be obtained by using the energy-balance analysis, using (23) and (24) for the antiparallel diodes and the transistors, respectively. The predicted efficiency curve as a function of the output power is depicted in Fig. 20(b) for both power devices. Additionally, an experimental prototype has been built for demonstrate the feasibility of the proposed design method featuring the IHW40N60R power device, which exhibits the best efficiency results. The measured efficiency results have been also included in Fig. 20(b). Finally, main converter waveforms at maximum (1 kW) and medium (0.5 kW) output power levels are depicted in Fig. 21. Additionally, the main power devices waveforms have been also included.

VI. Conclusion

In this paper, an analytical model of the half-bridge series resonant inverter has been proposed. One of the most important contributions of this model is that results are directly obtained

from closed-form expressions, reducing simulation time and enabling real-time control and emulation techniques.

The main waveforms of the converter are directly calculated, allowing extract control parameters required to operate the desired switching mode. In addition, a closed-form expression of the output power has been also obtained as a function of the main control parameters, valid for any modulation profile.

The main converter power loss has been studied. On the one hand, an analytical model has been obtained for conduction losses, proving that conduction efficiency is constant with output power and only depends on the load, supply voltage, and conduction parameters of the switching devices. On the other hand, an analytical model for the switching losses, focused on the ZVS mode, has also been obtained.

The analytical model presented in this paper has been verified experimentally through an induction heating inverter, showing a good agreement between theoretical and experimental results. Besides, a design example of a resonant inverter for induction heating applications taking advantage of the proposed model has been detailed. These results prove the accuracy of the proposed model and its suitability as a tool to improve both the design process and the converter operation.

REFERENCES

[1] F. Weiyi, F. C. Lee, and P. Mattavelli, "Optimal trajectory control of LLC resonant converters for LED PWM dimming," *IEEE Trans. Power Electron.*, vol. 29, no. 2, pp. 979–987, Feb. 2014.

[2] H. Sarnago, O. Lucía, A. Mediano, and J. M. Burdío, "Multi-MOSFET-based series resonant inverter for improved efficiency and power density induction heating applications," *IEEE Trans. Power Electron.*, vol. 29, no. 8, pp. 4301–4312, Aug. 2014.

[3] J. Jordan, V. Esteve, E. Sanchis-Kilders, E. J. Dede, E. Maset, J. B. Ejea, and A. Ferreres, "A comparative performance study of a 1200 V Si and SiC MOSFET intrinsic diode on an induction heating inverter," *IEEE Trans. Power Electron.*, vol. 29, no. 5, pp. 2550–2562, May 2014.

[4] F. Weiyi, F. C. Lee, and P. Mattavelli, "Simplified optimal trajectory control (SOTC) for LLC resonant converters," *IEEE Trans. Power Electron.*,a vol. 28, no. 5, pp. 2415–2426, May 2013.

[5] H. Sarnago, O. Lucia Gil, A. Mediano, and J. Burdio, "Class-D/DE dual-mode-operation resonant converter for improved-efficiency domestic induction heating system," *IEEE Trans. Power Electron.*, vol. 28, no. 3, pp. 1274–1285, Mar. 2013.

[6] R. King and T. A. Stuart, "A normalized model for the half-bridge series resonant converter," *IEEE Trans. Aerosp. Electron. Syst.*, vol. AES-17, no. 2, pp. 190–198, Mar. 1981.

[7] H. Koizumi, K. Kurokawa, and S. Mori, "Analysis of class D inverter with irregular driving patterns," *IEEE Trans. Circuits Syst. I, Reg. Papers*, vol. 53, no. 3, pp. 677–687, Mar. 2006.

[8] M. K. Kazimierczuk and D. Czarkowski, *Resonant Power Converters*. New York, NY, USA: Willey, 2011.

[9] O. Pop and A. Taut, "Analysis and simulation of a half-bridge inverter," in *Proc. 32nd Int. Spring Semin. Electron. Technol.*, 2009, pp. 1–5.

[10] M. Hong, D. Songquan, w. Yangyang, and B. Issa, "Unified steady-state model and DC analysis of half-bridge DC-DC converters with current doubler rectifier," in *Proc. Appl. Power Electron. Conf. Expo.*, 2004, vol. 2, pp. 786–791.

[11] A. S. Kislovski, "A contribution to steady-state modeling of half-bridge series-resonant power cells," *IEEE Trans. Power Electron.*, vol. PE-1, no. 3, pp. 161–166, Jul. 1986.

[12] H. SarnagoAndia, A. Mediano, and O. Lucia, "High efficiency AC-AC power electronic converter applied to domestic induction heating," *IEEE Trans. Power Electron.*, vol. 27, no. 8, pp. 3676–3684, Aug. 2012.

[13] T. Mishima and M. Nakaoka, "A load-power adaptive dual pulse modulated current phasor-controlled ZVS high-frequency resonant inverter for induction heating applications," *IEEE Trans. Power Electron.*, vol. 29, no. 8, pp. 3864–3888, Aug. 2014.

[14] F. F. A. van der Pijl, M. Castilla, and P. Bauer, "Adaptive sliding-mode control for a multiple-user inductive power transfer system without need for communication," *IEEE Trans. Ind. Electron.*, vol. 60, no. 1, pp. 271–279, Jan. 2013.

[15] D. Paesa, C. Franco, S. Llorente, G. Lopez-Nicolas, and C. Sagues, "Adaptive simmering control for domestic induction cookers," *IEEE Trans. Ind. Appl.*, vol. 47, no. 5, pp. 2257–2267, Sep./Oct. 2011.

[16] O. Lucía, J. M. Burdío, I. Millán, J. Acero, and D. Puyal, "Load-adaptive control algorithm of half-bridge series resonant inverter for domestic induction heating," *IEEE Trans. Ind. Electron.*, vol. 56, no. 8, pp. 3106–3116, Aug. 2009.

[17] O. Jiménez, O. Lucia, I. Urriza, L. A. Barragán, P. Mattavelli, and D. Boroyevich, "FPGA-based gain-scheduled controller for resonant converters applied to induction cooktops," *IEEE Trans. Power Electron.*, vol. 29, no. 4, pp. 2143–2152, Apr. 2014.

[18] Y. Chen and V. Dinavahi, "Digital hardware emulation of universal machine and universal line models for real-time electromagnetic transient simulation," *IEEE Trans. Ind. Electron.*, vol. 59, no. 2, pp. 1300–1309, Feb. 2012.

[19] M. Aung and V. Dinavahi, "FPGA-based real-time emulation of power electronic systems with detailed representation of device characteristics," *IEEE Trans. Ind. Electron.*, vol. 58, no. 1, pp. 358–368, Jan. 2011.

[20] O. Lucía, I. Urriza, L. A. Barragan, D. Navarro, O. Jiménez, and J. M. Burdío, "Real-time FPGA-based hardware-in-the-loop simulation testbench applied to multiple output power converters," *IEEE Trans. Ind. App.*, vol. 47, no. 2, pp. 853–860, Mar./Apr. 2011.

[21] O. Jimenez, O. Lucia, I. Urriza Parroque, L. A. Barragan, D. Navarro, and V. Dinavahi, "Implementation of an FPGA-based on-line hardware-in-the-loop emulator using high-level synthesis tools for resonant power converters applied to induction heating appliances," *IEEE Trans. Ind. Electron.*, to be published.

[22] F. Forest, S. Faucher, J.-Y. Gaspard, D. Montloup, J.-J. Huselstein, and C. Joubert, "Frequency-synchronized resonant converters for the supply of multiwindings coils in induction cooking appliances," *IEEE Trans. Ind. Electron.*, vol. 54, no. 1, pp. 441–452, Feb. 2007.

[23] F. Forest, E. Labouré, F. Costa, and J.-Y. Gaspard, "Principle of a multi-load/single converter system for low power induction heating," *IEEE Trans. Ind. Electron.*, vol. 15, no. 2, pp. 223–230, Mar. 2000.

[24] D. Puyal, C. Bernal, J. M. Burdio, I. Millan, and J. Acero, "A new dynamic electrical model of domestic induction heating loads," in *Proc. IEEE Appl. Power Electronics Conf. Expo.*, 2008, pp. 409–414.

[25] C. Carretero, O. Lucía, J. Acero, R. Alonso, and J. M. Burdío, "Frequency-dependent modeling of domestic induction heating systems using numerical methods for accurate time-domain simulation," *IET Power Electron.*, vol. 5, pp. 1291–1297, Sep. 2012.

[26] P. Fu-Sheng, O. Chung-Lun, and H. Shyh-Jier, "Plasma-driven system circuit design with asymmetrical pulsewidth modulation scheme," *IEEE Trans. Ind. Electron.*, vol. 58, no. 9, pp. 4167–4174, Sep. 2011.

[27] O. Lucía, J. M. Burdío, I. Millán, J. Acero, and L. A. Barragán, "Efficiency oriented design of ZVS half-bridge series resonant inverter with variable frequency duty cycle control," *IEEE Trans. Power Electron.*, vol. 25, no. 7, pp. 1671–1674, Jul. 2010.

[28] I. Millán, D. Puyal, J. M. Burdío, O. Lucía, and D. Palacios, "IGBT selection method for the design of resonant converters for domestic induction heating," in *Proc. Eur. Conf. Power Electron. Appl.*, 2009, pp. 1–7.

[29] Q. Jinrong, A. Khan, and I. Batarseh, "Turn-off switching loss model and analysis of IGBT under different switching operation modes," in *Proc. IEEE 21st Int. Conf. Ind. Electron., Control, Instrum.*, vol. 1, 1995, pp. 240–245.

[30] J. Shiqi, L. Ting, Z. Zhengming, Y. Hualong, Y. Liqiang, Y. Sheng, and C. Secrest, "Physical model analysis during transient for series-connected HVIGBTs," *IEEE Trans. Power Electron.*, vol. 29, no. 11, pp. 5727–5737, Nov. 2014.

[31] L. Meng, K. Cheng, and K. Chan, "Systematic approach to high-power and energy-efficient industrial induction cooker system: Circuit design, control strategy and prototype evaluation," *IEEE Trans. Power Electron.*, vol. 26, no. 12, pp. 3754–3765, Dec. 2011.

[32] J. Acero, C. Carretero, I. Millán, O. Lucía, R. Alonso, and J. M. Burdío, "Analysis and modeling of planar concentric windings forming adaptable-diameter burners for induction heating appliances," *IEEE Trans. Power Electron.*, vol. 26, no. 5, pp. 1546–1558, May 2011.

[33] O. Lucía, J. M. Burdío, I. Millán, J. Acero, and L. A. Barragán, "Efficiency oriented design of ZVS half-bridge series resonant inverter with variable frequency duty cycle control," *IEEE Trans. Power Electron.*, vol. 25, no. 7, pp. 1671–1674, Jul. 2010.

[34] O. Jiménez, O. Lucía, L. A. Barragán, D. Navarro, J. I. Artigas, and I. Urriza, "FPGA-based test-bench for resonant inverter load characterization," *IEEE Trans. Ind. Informat.*, vol. 9, no. 3, pp. 1645–1654, Aug. 2013.
[35] O. Lucía, J. M. Burdío, I. Millán, J. Acero, and D. Puyal, "Load-adaptive control algorithm of half-bridge series resonant inverter for domestic induction heating," *IEEE Trans. Ind. Electron.*, vol. 56, no. 8, pp. 3106–3116, Aug. 2009.
[36] O. Lucía, J. M. Burdío, L. A. Barragán, J. Acero, and I. Millán, "Series-resonant multiinverter for multiple induction heaters," *IEEE Trans. Power Electron.*, vol. 25, no. 11, pp. 2860–2868, Nov. 2010.

Héctor Sarnago (M'09) received the M.Sc. degree in electrical engineering from the University of Zaragoza, Zaragoza, Spain, in 2010. He is currently working toward the Ph.D. degree from the same institution.

He is with the Department of Electronic Engineering and Communications, University of Zaragoza. His main research interests include resonant converters and digital control for induction heating applications.

Mr. Sarnago is a Member of the Aragon Institute for Engineering Research (I3A).

Óscar Lucía (S'04–M'11–SM'14) received the M.Sc. and Ph.D. degrees (with Hons.) in electrical engineering from the University of Zaragoza, Zaragoza, Spain, in 2006 and 2010, respectively.

During 2006 and 2007, he held a Research Internship at the Bosch and Siemens Home Appliances Group. Since 2008, he has been with the Department of Electronic Engineering and Communications, University of Zaragoza, where he is currently an Assistant Professor. During part of 2009 and 2012, he was a Visiting Scholar at the Center of Power Electronics Systems (CPES), Virginia Tech. His main research interests include resonant power conversion, wide-bandgap devices, and digital control, mainly applied to contactless energy transfer and induction heating applications. In these topics, he has published more than 40 international journal papers and 100 conference papers, and he has filed more than 25 patents.

Dr. Lucía is a Member of the Aragon Institute for Engineering Research (I3A) and an active member of the Power Electronics (PELS) and Industrial Electronics (IES) societies. During 2013, he was a Guest Associate Editor of the IEEE TRANSACTIONS ON INDUSTRIAL ELECTRONICS. Since 2014, he has been an Associate Editor of the IEEE TRANSACTIONS ON INDUSTRIAL ELECTRONICS.

Arturo Mediano (M'98–SM'06) received the M.Sc. and the Ph.D. degrees in electrical engineering from the University of Zaragoza, Spain, in 1990 and 1997, respectively.

Since 1992, he has been a Professor with special interests in RF (HF/VHF/UHF) and EMI/EMC design for Telecom and Electrical Engineers. From 1990, he has been involved in design and management responsibilities for research and development projects in the RF field for communications, industry, and scientific applications. His research interest include high-efficiency switching mode RF power amplifiers, where he has experience in applications like broadcast, mobile communication radios, through-earth communication systems, induction heating, plasmas for industrial applications and RFID. He has a solid experience in collaboration with industry (including training and consultancy in RF and EMI/EMC).

Dr. Mediano is an active member from 1999 and currently the Vicechair of the MTT-17 (HF/VHF/UHF technology) Technical Committee of the Microwave Theory and Techniques Society of the IEEE.

José M. Burdío (M'97–SM'12) received the M.Sc. and Ph.D. degrees in electrical engineering from the University of Zaragoza, Zaragoza, Spain, in 1991 and 1995, respectively.

He has been with the Department of Electronic Engineering and Communications at the University of Zaragoza, where he is currently a Professor. His main research interests include modeling of switching converters and resonant power conversion for induction heating applications.

Dr. Burdío is a Member of the Aragon Institute for Engineering Research (I3A).